**RESEARCH ARTICLE**

NANO · MICRO small
www.small-journal.com

# Flexible Block Copolymer Metamaterials Featuring Hollow Ordered Nanonetworks with Ultra-High Porosity and Surface-To-Volume Ratio

*I-Ming Lin, Chih-Ying Yang, Yi-Ming Wang, Wei-En Wang, Yu-Chueh Hung, Edwin L. Thomas, and Yeo-Wan Chiang**

**By utilizing bicontinuous and nanoporous ordered nanonetworks, such as double gyroid (DG) and double diamond (DD), metamaterials with exceptional optical and mechanical properties can be fabricated through the templating synthesis of functional materials. However, the volume fraction range of DG in block copolymers is significantly narrow, making it unable to vary its porosity and surface-to-volume ratio. Here, the theoretically limited structural volume of the DG phase in coil-coil copolymers is overcome by enlarging the conformational asymmetry through the association of mesogens, providing fast access to achieving flexible structured materials of ultra-high porosities. The new materials design, dual-extractable nanocomposite, is created by incorporating a photodegradable block with a solvent-extractable mesogen (m) into an accepting block, resulting in a new hollow gyroid (HG) with the largely increased surface-to-volume ratio and porosity of 77 vol%. The lightweight HG exhibits a low refractive index of 1.11 and a very high specific reduced modulus, almost two times that of the typical negative gyroid (porosity≈53%) and three times that of the positive gyroid (porosity≈24%). This novel concept can significantly extend the DG phase window of block copolymers and the corresponding surface-to-volume ratio, being applicable for nanotemplate-synthesized nanomaterials with a great gain of mechanical, catalytic, and optoelectronic properties.**

## 1. Introduction

Ordered nanoporous network structures created through self-assembly are interesting nanosized inorganic and organic materials in themselves, but they can also be used to produce nanotemplates featuring high surface-to-volume ratios. Indeed, three-dimensional (3-D) porous nanostructures featuring highly interconnected microdomains, made from the ordered gyroid phases of self-assembled block copolymers (BCPs) containing uniformly bicontinuous microdomains,[1–3] have found diverse applications in catalysis, separation, nanoreactors, optoelectronic devices, and photonic crystals.[4–7] For example, gyroid-structured metal-oxide materials formed through the replication of nanoporous gyroid structures are useful materials in solar cells, electrochromic devices, and photocatalysts because of their high porosity, high surface-to-volume ratio and excellent mechanical properties.[8–10] As illustrated in **Figure** 1b, a double gyroid (DG) phase consists of two independent and catenated nanonetworks including one left-handed and one right-handed frameworks embedded in a majority matrix. The volume fraction of the nanonetworks in diblock copolymers is typically ≈0.33–0.42.[6,11,12] A positive double gyroid (PG) nanoporous structure is obtained upon removal of the two independent minor nanonetworks to form gyroid channels (Figure 1c). In contrast, removing the major matrix forms a negative double gyroid (NG) nanoporous structure (i.e., a gyroid network; Figure 1d). Accordingly, PG and NG nanoporous structures have typically possessed porosities of ≈33–42 and 58–67%, respectively. The PG channel in the matrix has frequently been obtained after the removal of the minor component from a semi-degradable BCP—for example, polystyrene-*block*-poly(ʟ-lactide) (PS-*b*-PLLA),[13,14] or polystyrene-*block*-polyisoprene (PS-*b*-PI).[15,16] In contrast, the NG structure is rarer and can be obtained after the removal of the major component from a semi-degradable BCP—for example, polystyrene-*block*-polyisoprene (PS-*b*-PI).[4] Therefore, most investigations have fabricated the NG network from the identical semi-degradable BCP by

I-M. Lin, Y.-M. Wang, Y.-W. Chiang
Department of Materials and Optoelectronic Science
National Sun Yat-Sen University
Kaohsiung 80424, Taiwan
E-mail: ywchiang@mail.nsysu.edu.tw

I-M. Lin, E. L. Thomas
Department of Materials Science & Engineering
Texas A&M University
College Station, TX 77843, USA

C.-Y. Yang, W.-E. Wang, Y.-C. Hung
Institute of Photonics Technologies
National Tsing Hua University
Hsinchu 300, Taiwan

The ORCID identification number(s) for the author(s) of this article can be found under https://doi.org/10.1002/smll.202307487

DOI: 10.1002/smll.202307487

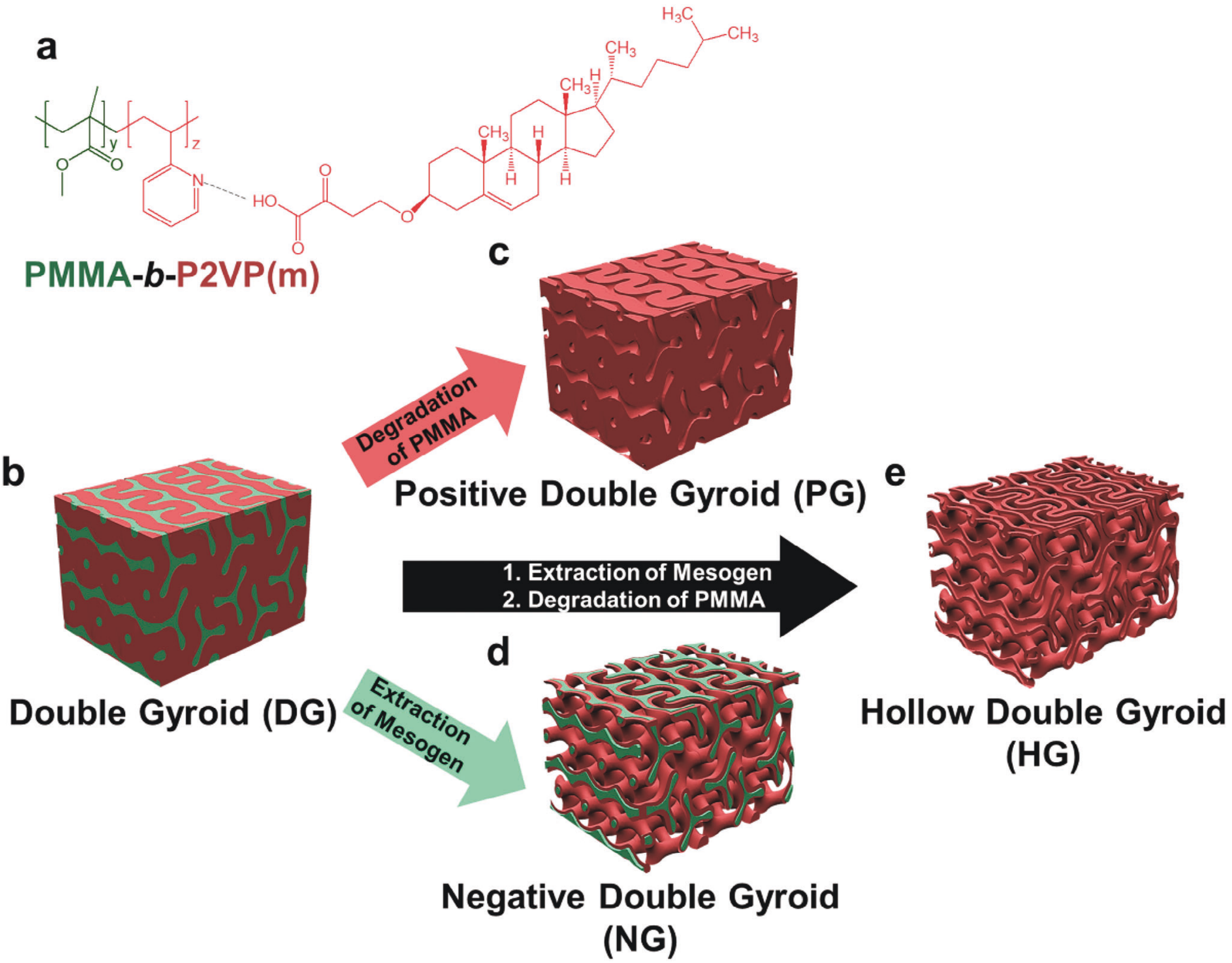

**Figure 1.** Schematic representation of a dual-extractable DG-forming nanocomposite for fabricating various ordered nanoporous network structures. a) Illustration of the PMMA-*b*-P2VP(m) nanocomposite. b) Microphase-separated DG structure formed from the copolymer/mesogen nanocomposite with dual-extractable characteristics. c) PG, d) NG, and e) HG nanoporous structures obtained after removal of the photodegradable PMMA component (green), the solvent-extractable liquid crystalline mesogen component (one of the two red matrix components), or both extractable PMMA and mesogen components, respectively.

templating synthesis involving multiple steps: preparation of the PG channel as a nanotemplate, infiltration of robust inorganic materials (e.g., metal or ceramic precursor materials) into the preformed PG channel, and extracting or calcination to remove the residual organic materials.[13,14,17–19] Such a multi-step complex process can result in the inefficient fabrication of distorted, rigid, and inorganic NG structures resulting from a series of incomplete infiltration steps and material shrinkage after calcination.

In this study, we developed a new dual-extractable ternary nanocomposite that allows the one-step fabrication of both the PG and NG nanostructures. This three-constituent and dual-extractable nanocomposite was formed from a single semi-degradable copolymer incorporated with extractable mesogens. In addition to PG and NG structures due to the extractable property, we could also fabricate a third novel nanoporous structure by this unique dual-extractable property—a hollow double gyroid (HG) nanostructure (Figure 1e) possessing ultrahigh porosity. Therefore, this novel approach could provide three different 3-D polymer-based nanotemplates from a single starting material system, subsequently enabling the templating synthesis of DG-shaped materials having ultrahigh surface-to-volume ratios, and nanoscale features with potential applications in catalysis, energy translation, energy conversion, and storage.

Figure 1a shows a blend of the semi-degradable BCP, poly(methyl methacrylate)-*block*-poly(2-vinyl pyridine) (PMMA-*b*-P2VP), with the cholesteric liquid crystal mesogen (m), cholesteryl hemisuccinate, resulting in a PMMA-*b*-P2VP(m)$_x$ nanocomposite where $x$ denotes the molar ratio of mesogen to P2VP monomer unit. Because of the strong hydrogen bonding interaction, the acid-functionalized cholesteric mesogens sequester selectively and exclusively into the P2VP microdomains.[20–23] Accordingly, we could fabricate nanoporous PG and NG nanostructures from the PMMA-*b*-P2VP(m)$_x$

nanocomposite through one-step degradation (UV irradiation) of the minor PMMA network[24] or through one-step removal (solvent extraction) of the mesogenic molecules from the P2VP(m)$_x$ matrix (Figure 1c,d).[25,26] Furthermore, because of the dual-extractable characteristic, we could also obtain a hollow double gyroid—namely, an HG structure—through the removal of both the PMMA block and the included mesogens (Figure 1e). Compared with the typical PG and NG, this ordered HG nanostructure has a maximum surface-to-volume ratio, an extremely low refractive index, and the highest transmittance,[27] suggesting potential applications in antireflective coatings [13] and the encapsulation of optical devices.[28] Furthermore, the highly efficient fabrication of PG, NG, and novel HG nanoporous templates from the dual-extractable ternary nanocomposite is excellent for synthesizing nanoscale materials with high specific modulus and large surface-to-volume ratio.

## 2. Results and Discussion

### 2.1. Conformational-Asymmetry-Induced Double Gyroid with a Minimum Structural Volume

The transmission electron microscopy (TEM) image in Figure S1a (Supporting Information) reveals the microphase-separated structure of the semi-degradable PMMA-*b*-P2VP BCP cast from 1,1,2-trichloroethane (TCE). We observe a lamellar morphology, consistent with the expected morphology of the BCP phase diagram having a PMMA volume fraction ($\phi_{\text{PMMA}}$) of 0.51. The corresponding small-angle X-ray scattering (SAXS) profile also reveals lamellar reflections, with a relative $q$ ratio of 1:2:3 (Figure S1d, Supporting Information). The lamellar periodicity calculated from the primary scattering peak was 64 nm.

The introduction of an additive that is highly compatible with one of the blocks can effectively manipulate the self-assembled morphology of such a copolymer featuring specific functionalities. Here, we added the acid-terminated mesogen, cholesteryl hemisuccinate, with the expectation that it would hydrogen bond to the P2VP block. Because of the reversible nature of the noncovalent bonding interaction, the mesogenic molecules are potentially extractable from the P2VP microdomains if they experience stronger polar interactions (e.g., when extracting using polar solvents). As a result, the PMMA-*b*-P2VP(m)$_x$ nanocomposite displays dual-extractable characteristics—photo-degradable PMMA blocks and solvent-extractable mesogens—to allow the preparation of three types of nanoporous structures. When we introduced a small amount of the mesogens to the PMMA-*b*-P2VP to form the PMMA-*b*-P2VP(m)$_{0.05}$ ($\phi_{\text{PMMA}}$ = 0.45) nanocomposite (here, 0.05 represents the mole fraction of the mesogen to the 2-vinylpyridine unit), we obtained a long-range-ordered lamellar morphology (Figure S1b, Supporting Information) with the appearance of several high-order reflections at a $q$ ratio of 1:2:3 in the SAXS profile (Figure S1d, Supporting Information). The lamellar periodicity of the PMMA-*b*-P2VP(m)$_{0.05}$ increased to 72 nm after introducing the mesogens. Increasing the amount of the mesogen component to $x = 0.2$ also resulted in a lamellar morphology with a periodicity of 98 nm even though the layer thickness ratio is highly asymmetric in the PMMA-*b*-P2VP(m)$_{0.2}$ ($\phi_{\text{PMMA}} = 0.34$) (Figure S1c,d, Supporting Information). With the increase of the molar ratio from 0 to 0.05 and 0.2, the domain size of the P2VP(m)$_x$ increases significantly from 31.4 to 39.6 and 64.7 nm, respectively (Figure S1e, Supporting Information). In contrast, the domain size of the PMMA (32.4–33.3 nm) is almost independent of the molar ratio. Interestingly, further increasing the quantity of the mesogen in the PMMA-*b*-P2VP(m)$_{0.45}$ ($\phi_{\text{PMMA}}$ = 0.24) led to a phase transition to the highly interconnected DG phase. **Figure** 2a shows the well-known two-fold projection structure of the bright-field TEM image along the [110] direction. The minor PMMA block ($\phi_{\text{PMMA}}$ = 0.24) formed a pair of DG networks embedded in the major P2VP(m)$_{0.45}$ matrix. The corresponding SAXS profile in Figure 2c shows Bragg peaks with the $q$ ratio of $\sqrt{6}$: $\sqrt{8}$: $\sqrt{20}$ (i.e., {211}, {220}, {420}), confirming the formation of the DG phase with a lattice parameter of 388 nm. The high-resolution TEM micrograph revealed (Figure 2b) that the PMMA network was surrounded by a smectic phase of the mesogens with homogeneous anchoring conditions such that the smectic layers are perpendicular to the intermaterial dividing surface (IMDS). As estimated, the black region of the P2VP block backbone layer and the white region of the mesogen domain are ≈1.9 and 2.6 nm, respectively (the inset in Figure 2b). In Figure 2d, the lamellar reflections with the ratio of 1: 2: 3 in the medium-angle X-ray diffraction (MAXD) profile indicate the formation of a smectic phase having a periodicity of 4.7 nm, almost identical to that measured by TEM. Similar phase transitions with the liquid crystalline mesophase can also be found in the case of low-molecular-weight amphiphilic liquid crystalline compounds.[29–32] The Kuhn lengths of P2VP and PMMA are 1.8 and 1.53 nm,[33,34] respectively, which are smaller than the structural length of the mesogen (2.2 nm). As the mesogen molecules are selectively introduced into the P2VP domain to form a comb-like chain structure, the P2VP chain becomes highly stretched as evidenced by the formation of the asymmetric lamellar structure previously. Therefore, the conformational asymmetry is significantly enhanced in the PMMA-*b*-P2VP(m) nanocomposite consistent with the expected shifting of the phase boundary in the asymmetric BCP.[35,36] In contrast to the typical volume fraction range of 0.33–0.42 to form a DG phase, the DG phase with such a low volume fraction ($\phi_{\text{PMMA}}$ = 0.24) has not been previously experimentally observed. Figure 2e shows the computer-generated triply periodic minimal surface (Schoen's G surface) with a constant thickness (CT) model by displacing the G surface along the local normal distance, creating a constant thickness ($h$) matrix domain. As shown, the perpendicular smectic layer phase (black and white fringes) is composed of the mesogens (purple ellipsoids) hydrogen-bonded to the stretched P2VP chains (red wires), forming a hierarchical lamellae-within-gyroid structure. The calculated h value of the PMMA-*b*-P2VP(m)$_{0.45}$ ($\phi_{\text{PMMA}}$ = 0.24) CT-matrix gyroid is 104.6 nm with a lattice parameter of 388 nm. The thickness h (104.6 nm) is 47.5 times the length of the mesogen (2.2 nm), suggesting a homogeneous boundary condition of the mesogen molecules parallel to the PMMA-*b*-P2VP IMDS as illustrated in Figure 2e. Additionally, Figure 2f,g shows the experimental and simulated TEM micrographs of the DG structure with [110] and [211] projections in PMMA-*b*-P2VP(m)$_{0.45}$ ($\phi_{\text{PMMA}}$ = 0.24). The domain thicknesses from the experimental and simulated results are consistent, confirming the DG with a minimum volume fraction of 0.24. Further increasing the mesogen content ($x$ = 0.6) led to a phase transition to hexagonally packed PMMA

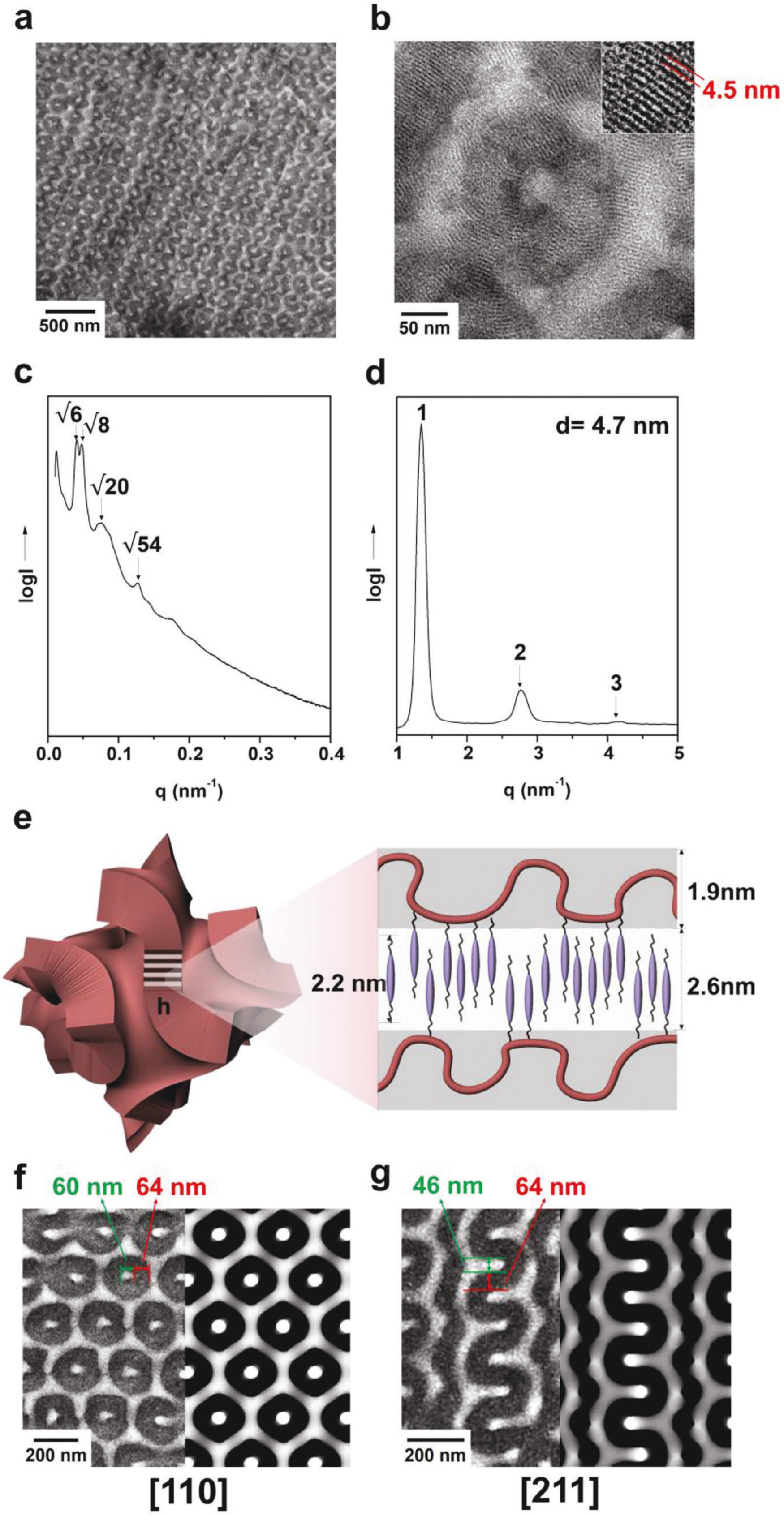
a
500 nm
b
4.5 nm
50 nm
c
√6
√8
√20
√54
logI
0.0
0.1
0.2
0.3
0.4
q (nm$^{-1}$)
d
1
d= 4.7 nm
2
3
logI
1
2
3
4
5
q (nm$^{-1}$)
e
h
1.9nm
2.2 nm
2.6nm
f
60 nm
64 nm
200 nm
[110]
g
46 nm
64 nm
200 nm
[211]

cylinders embedded in the P2VP(m) matrix ($\phi_{\mathrm{PMMA}}$ = 0.20) (Figure S2a,c, Supporting Information). The high-resolution TEM photograph (Figure S2b, Supporting Information) revealed that the PMMA cylinders were encircled by a perpendicular smectic phase again with the homogeneous boundary condition, forming a hierarchical cylinder-within-lamellae structure as verified by the MAXD profile showing the 1: 2: 3 reflections from the smectic layers (Figure S2d, Supporting Information). Notably, the self-assembled structure is strongly dependent on the solvent quality. We also tested different solvents, such as acetic acid and chloroform, to prepare PMMA-*b*-P2VP and PMMA-*b*-P2VP(m). In Figure S3a (Supporting Information), because acetic acid is a selective solvent for P2VP, PMMA micelles embedded in the P2VP matrix are observed in the neat PMMA-*b*-P2VP. After introducing the mesogen into PMMA-*b*-P2VP(m)$_{0.45}$, we still observed PMMA micelles in the P2VP(m) matrix (Figure S3c, Supporting Information). In contrast, using chloroform, a neutral solvent but slightly selective to PMMA, we obtained the lamellar morphology in the neat PMMA-*b*-P2VP (Figure S3b, Supporting Information). In PMMA-*b*-P2VP(m)$_{0.45}$, we obtained PMMA cylinders in the P2VP(m) matrix (Figure S3d, Supporting Information).

The hydrogen bonding interaction in the PMMA-*b*-P2VP(m)$_x$ system was investigated using Fourier transform infrared spectrometer (FT-IR). The FT-IR spectra ranging from 1620 to 1575 cm$^{-1}$ (Figure S4a, Supporting Information) and from 1020 to 980 cm$^{-1}$ (Figure S4b, Supporting Information) show the absorption bands of the pyridine ring of the P2VP block chain. The neat PMMA-*b*-P2VP exhibits absorption bands at 1591 and 993 cm$^{-1}$, representing free pyridine units. After introducing the mesogen ($x$ = 0.05), a new absorption peak appears at 1601 cm$^{-1}$ (Figure S4a, Supporting Information) and 1009 cm$^{-1}$ (Figure S4b, Supporting Information), indicating the formation of hydrogen-bonded associations between P2VP and the mesogen. With an increase in the molar ratio to $x = 0.2$ and 0.45, the intensity of free pyridine absorption peaks at 1591 and 993 cm$^{-1}$ reduced, while hydrogen-bonded stretching at 1601 and 1009 cm$^{-1}$ increased. In Figure S4c (Supporting Information), the high-wavenumber FT-IR spectra ranging from 1760 to 1680 cm$^{-1}$ reveal C═O stretching signals from PMMA and the mesogen. The neat PMMA-*b*-P2VP shows an absorption band at 1727 cm$^{-1}$ attributed to the free C═O group in PMMA. The mesogen exhibits three absorption peaks at 1708, 1724, and 1732 cm$^{-1}$. The absorption at 1732 cm$^{-1}$ is due to the free C═O group in the mesogen. The absorption bands at 1724 and 1708 cm$^{-1}$ are attributed to the dimerization of mesogens. In the PMMA-*b*-P2VP(m)$_x$ ($x = 0.05$, 0.2, and 0.45), the absorption band at 1727 cm$^{-1}$ with a shoulder at 1732 cm$^{-1}$ indicates that all C═O groups are free of hydrogen bonds. This indicates that mesogens do not form hydrogen bonds with PMMA. As a result, this confirms the strong hydrogen bonding interaction between the pyridine of P2VP and the carboxylic acid of the mesogen in PMMA-*b*-P2VP(m) systems.

### 2.2. Various Nanoporous Double Gyroids from the Dual-Extractable Nanocomposite

Taking advantage of the photodegradability of the PMMA block and the solvent extractability of the mesogen, we can obtain three different types of nanoporous DG structures—PG, NG, and HG—from this dual-extractable PMMA-*b*-P2VP(m)$_{0.45}$ nanocomposite. UV irradiation at 254 nm for 4 h triggered the depolymerization of the PMMA blockchains and the cross-linking of the P2VP blockchains.[37] To remove the photodegraded PMMA blocks, we immersed the exposed PMMA-*b*-P2VP(m)$_{0.45}$ nanocomposite into o-xylene, a poor solvent for the P2VP and the mesogen. In **Figure 3**a, the field-emission scanning electron microscope (FESEM) image reveals the PG nanochannels viewed along the [110] direction. In Figure 3b, the corresponding SAXS profile with the $q$ ratio of $\sqrt{6}$: $\sqrt{8}$ reveals that the DG structure is retained with a lattice parameter of 381 nm after the removal of the minor PMMA, indicating a slight shrinkage compared with the lattice parameter of the original DG phase (388 nm) (**Table 1**). In contrast, direct immersion of the DG-forming PMMA-*b*-P2VP(m)$_{0.45}$ nanocomposite in methanol for 1 h disassociated the hydrogen-bonded mesogens from the P2VP blockchains, leading to contraction of the P2VP chains. Accordingly, we obtained a nanoporous NG structure consisting of the PMMA networks surrounded by the collapsed P2VP blockchains after the removal of the mesogens through the solvent-extracting treatment (Figure 3c). Figure S5 (Supporting Information) reveals a corresponding TEM micrograph of the NG featuring the core(PMMA)–shell(P2VP) networks. Due to the lack of an intermediate supporting matrix after removing the mesogens, the two networks of NG may shift vertically due to gravity. As a result, the shifted NG behaves a single-gyroid-like structure, resulting in a new set of forbidden {110} reflections at a relative $q$ position of $\sqrt{2}$ (Figure 3d).[13] Also, the lattice parameter of 379 nm (Table 1) of the NG phase suggests only a slight shrinkage after the extraction of the mesogen.

Next, we applied methanol-extraction of the mesogen followed by UV irradiation and o-xylene-extraction for removing PMMA to obtain a HG nanonetwork consisting of the P2VP block only—the first example of a polymer-based HG structure. After the removal of both the PMMA blocks and the mesogen, the high-magnification FESEM micrograph in Figure 3e displays the HG networks revealing the translational shifting of the two networks after the removal of the mesogen. Similar to NG, this shifting of the two networks results in a change of space group from Ia3d to I4132 and the appearance of the forbidden {110} reflection

**Figure 2.** a) TEM micrograph of PMMA-*b*-P2VP(m)$_{0.45}$. b) High-resolution TEM micrograph of a portion of Figure (a). The inset in Figure (b) shows the smectic phase of the P2VP(m)$_{0.45}$ nanodomains. After I$_2$ staining, the P2VP(m)$_{0.45}$ microdomains appear dark and the PMMA microdomains are bright. The corresponding c) SAXS and d) MAXD profiles of the PMMA-*b*-P2VP(m)$_{0.45}$. Multiple Bragg peaks with an integer ratio of 1: 2: 3 in the MAXD profile of PMMA-*b*-P2VP(m)$_{0.45}$ indicate the formation of a smectic phase in the matrix region of the DG structure. e) Schematic representation of the constant thickness (CT) model for the DG matrix with thickness f) consisting of the P2VP block backbone layer (black) and the mesogen layer (white). Experimental and simulated TEM micrographs of the projections normal to the f) [110] and g) [211] planes of the DG phase having the network volume fractions of 0.24 in PMMA-*b*-P2VP(m)$_{0.45}$. The projected thicknesses of the bright and dark domains in the [110] plane are 60 and 64 nm, respectively; the bright and dark domains in the [211] plane are 46 and 64 nm, respectively.

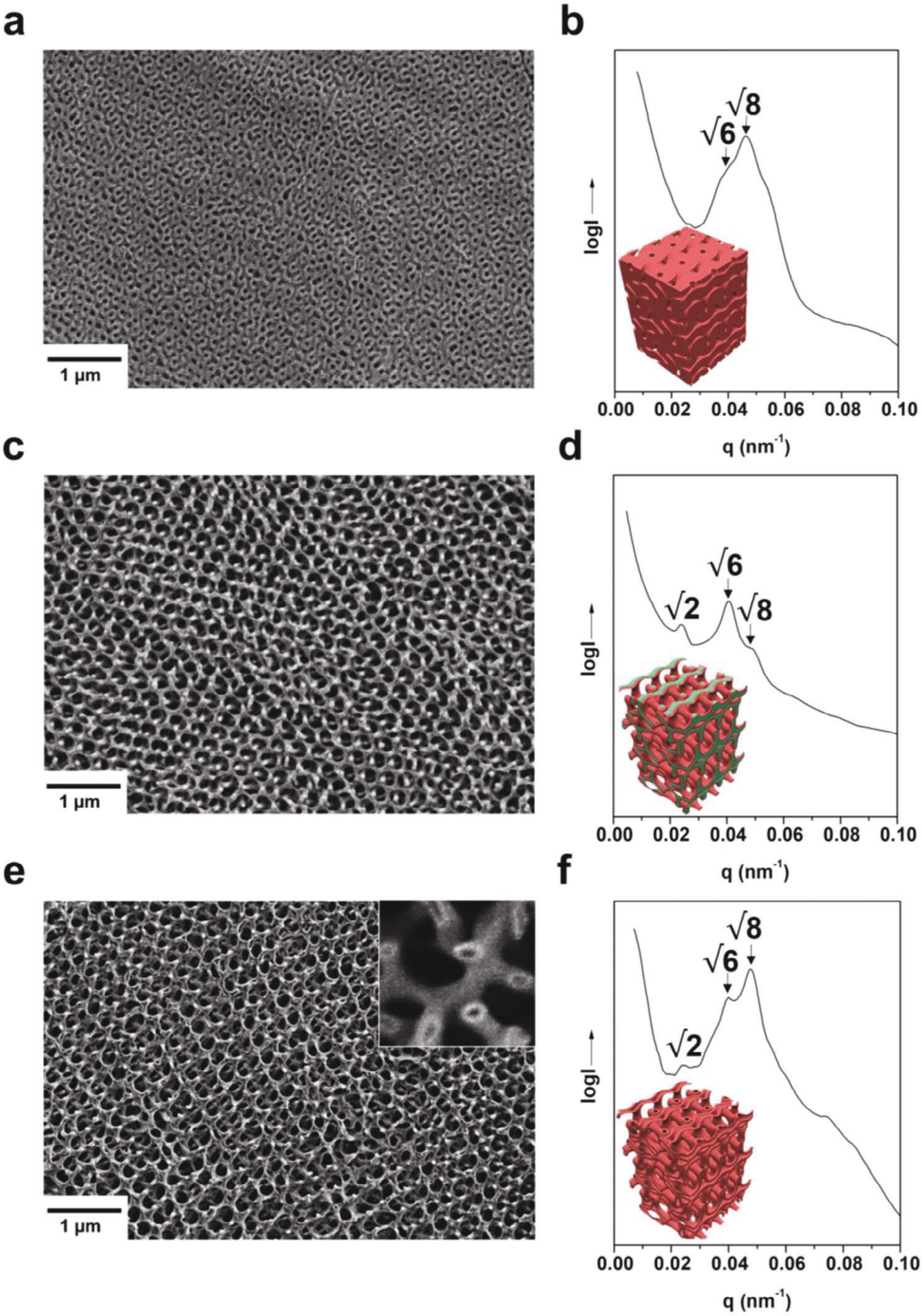

**Figure 3.** FESEM micrographs and the corresponding SAXS profiles of the various nanoporous DG structures from the PMMA-*b*-P2VP(m)$_{0.45}$ ternary nanocomposite. a,b) PG, c) and d) NG, and e) and f) HG nanoporous structures obtained after removal of the PMMA, the mesogens, or both PMMA and mesogens, respectively. The inset in Figure (e) is a high-magnification image of the porous HG network. The appearance of the $\sqrt{2}$ reflections in Figures (d) and (f) is attributed to the shifting of the two networks after removing the mesogens from the matrix.

at a relative $q$ position of $\sqrt{2}$ in the corresponding SAXS profile (Figure 3f). The estimated thickness of the P2VP shell and the diameter of the air core are ≈19.4 and 30.6 nm, respectively. Since the two networks are nanoporous and of a low volume fraction, we estimated the S/V value using a double-level set model with a volume fraction of 23%. Here, the bulk volumes ($V_{\mathrm{bulk}}$) of the PG, NG, and HG are calculated according to the corresponding (100) cubic unit cell lattice parameters, and the computational surface areas of the porous NG and HG are shown in **Figure 4a–d**. The calculated surface-to-volume ratios (S/V) are shown in **Table 2**.

**Table 1.** Characteristics of nanoporous DG structures.

| Sample | Volume Fraction | | | | $d_{(100)}$ [nm] | Calculated $\rho$ [g cm$^{-3}$]$^{a)}$ | $\rho$ [g cm$^{-3}$] |
|---|---|---|---|---|---|---|---|
| | PMMA | P2VP | m | air | | | |
| DG PMMA-P2VP(m)$_{0.45}$ | 0.24 | 0.23 | 0.53 | 0 | 388 | 1.11 | 1.11 |
| PG Air-P2VP(m)$_{0.45}$ | 0 | 0.23 | 0.53 | 0.24 | 381 | 0.82 | 0.82$^{b)}$ |
| NG PMMA-*b*-P2VP(Air) | 0.24 | 0.23 | 0 | 0.53 | 379 | 0.55 | 0.55$^{b)}$ |
| HG Air-P2VP(Air) | 0 | 0.23 | 0 | 0.77 | 378 | 0.27 | 0.26$^{b)}$ |
| PMMA | | | | | | | 1.188 |
| P2VP | | | | | | | 1.153 |
| mesogen (m) | | | | | | | 1.06 |

[a)] Calculated by using the preserved volume fraction of the various DG-forming structures and the density of PMMA, P2VP, and mesogen. [b)] The density is calculated by the residual weight after extraction of PMMA, P2VP, or both components, divided by the sample volume estimated from the measured lattice parameter from SAXS.

As listed, the $V_{\text{bulk}}$ of the PG, NG, and HG are similar due to their nearly constant lattice parameters. As anticipated, the surface area (S) of the HG is almost identical to the sum of those of the NG and PG. Therefore, the S/$V_{\text{bulk}}$ of HG (0.0251 nm$^{-1}$) is also similar to the sum of S/$V_{\text{bulk}}$s of NG (0.0141 nm$^{-1}$) and PG (0.0111 nm$^{-1}$). In addition, if we consider the preserved actual volume ($V_p$), the surface-to-volume ratio (S/$V_p$) of the HG (0.119 nm$^{-1}$) is 8.2 times and 4.0 times higher than that of PG (0.0145 nm$^{-1}$) and NG (0.0300 nm$^{-1}$), respectively. Figure 4e and Figure S6 (Supporting Information) show the simulated surface properties of PG, NG, and HG made from DG with varying lattice parameters ($d_{100}$). As the lattice size decreases, the surface-to-volume ratio and the specific surface area both increase. Among them, the increment in HG increases much more significantly. Simulated results demonstrate that the HG phase can exhibit a specific surface area of 97 m$^2$ g$^{-1}$, or even higher values using lower-Mw PMMA-*b*-P2VP BCPs (Figure 4e). This indicates that HG structures made by PMMA-*b*-P2VP or semi-degradable amphiphilic diblock copolymers of different Mws have potential applications in various fields. The HG structure from the dual–extractable DG-forming ternary nanocomposite of the minimum structural volume possesses a maximum porosity that is not achievable by the usual approach for making either an NG or PG structure from the typical semi-degradable diblock copolymers.

We conducted $^1$H NMR measurements for the mesogen, DG, and NG with various extraction times (Figure S7a, Supporting Information). The main signals related to the hydrogen bonding interaction and the existence of the mesogen are presented in the ranges of 8–8.5 ppm (Figure S7b, Supporting Information) and 5.1–5.7 ppm (Figure S7c, Supporting Information), respectively. In Figure S7b (Supporting Information), in contrast to the neat PMMA-b-P2VP, the up-field chemical shifts in 8.06, 8.14, and 8.21 ppm (indicated by red dashed line) are observed in the DG sample, corresponding to the proton next to the N atom in P2VP (labeled as h) due to hydrogen-bonding interaction with the mesogen. After extracting the mesogen by immersing the DG sample in methanol for 10 min, the signals return to that of the neat sample in 8.07, 8.15, and 8.22 ppm (indicated by black dashed lines) in Figure S7b (Supporting Information), indicating the complete removal of the mesogen. Similar signals are obtained for a longer extraction time of 30 min. This can also be confirmed by the silent signal of the mesogen at 5.37 ppm corresponding to the proton labeled as *i* after being immersed in ethanol for 10 and 30 min in Figure S7c (Supporting Information). As a result, the mesogen can be entirely removed after immersion in methanol for 10 min. Notably, the $^1$H NMR spectra of the HG sample cannot be measured due to insolubility in D-chloroform resulting from photoirradiation-induced crosslinking of the P2VP blockchains. Therefore, we utilized FT-IR measurement to probe the removal of the PMMA as an alternative. In Figure S8 (Supporting Information), the absorption band at 1727 cm$^{-1}$ is assigned to the C=O group of PMMA. The intensity of this absorption decreased gradually after UV irradiation for 1 and 2 h followed by the extraction with o-xylene. After UV irradiation for 4 h, the absorption vanished, indicating the complete removal of PMMA.

The changes in components of PMMA-*b*-P2VP(m)$_{0.45}$ were also investigated using FT-IR. In Figure S9a (Supporting Information), the DG and NG exhibit the absorption band at 1727 cm$^{-1}$, confirming the presence of PMMA. Similar absorption in the PG is due to the presence of the mesogen. In Figure S9b (Supporting Information), the DG exhibits two absorption bands at 1591 and 1601 cm$^{-1}$, indicating the presence of free and hydrogen-bonded pyridines, respectively. The PG shows similar two absorption bands at 1591 and 1601 cm$^{-1}$ after removing PMMA. In contrast, the NG only shows the free pyridine absorption at 1591 cm$^{-1}$, suggesting the complete extraction of the mesogen. The HG only reveals the free pyridine P2VP absorption at 1591 cm$^{-1}$ without any absorption of C=O stretching at 1760 to 1680 cm$^{-1}$, further confirming the complete extraction of both PMMA and the mesogen after the dual extraction process.

### 2.3. Enhanced Performance of Nanoporous Double Gyroids

Because of high porosity, we expected the polymer-based HG to exhibit a very low refractive index without scattering visible light due to the nano-length scale of the structure. Based on the refractive index of the P2VP (1.59 at 600 nm) and the corresponding volume fraction of 0.23, we estimated the effective average refractive index of the HG network as 1.12, consistent with that (1.11) found by the experimental measurement via ellipsometry (Table S1, Supporting Information). **Figure** 5a presents the normal-incident transmittance spectra of various DG-forming structures. Due to the increased volume fraction of air, the transmittance increased upon proceeding from the PG structure ($\phi_{\text{air}} = 0.24$) to the NG structure ($\phi_{\text{air}} = 0.53$) and to the HG structure ($\phi_{\text{air}} = 0.77$). Furthermore, the HG film displayed low reflectivity and absorption (Figure 5b) in the visible range. Among these materials, the HG structure possessed the lowest volume fraction and the highest transmission (98%) in the visible range. As expected, there is a clear trend: increasing the volume fraction of air for the DG-forming structures having values of $\phi_{\text{air}}$ of 0, 0.24, 0.53, and 0.77 resulted in the increased transmittance (at 600 nm) from 0.90 to 0.93, 0.95, and 0.98, respectively. Consequently, the P2VP-based HG films were highly transparent and had very low reflectance

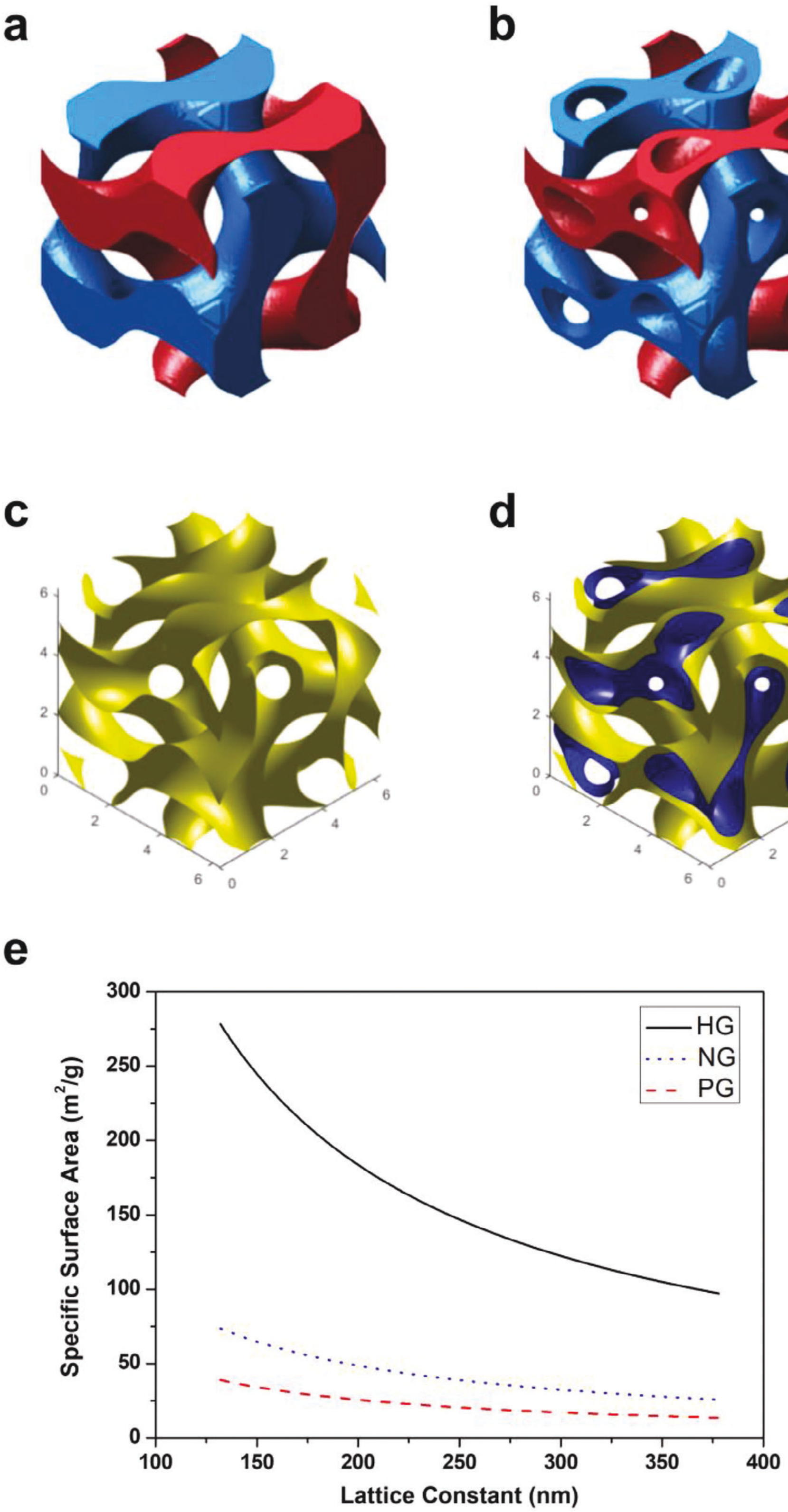

**Figure 4.** The computational preserved unit cell volume (Vp) of a) NG and b) HG. The corresponding computational surface area (S) of c) NG with a volume fraction of 47% and d) HG with a volume fraction of 23%. Figure (c) is a surface rendering of Figure (a), and Figure (d) is the surface rendering of the pair of nested surfaces in Figure (b). e) The simulated specific surface area of PG, NG, and HG varied with the lattice constant. The density of PG, NG, and HG used in the calculation of Figure (e) is 0.82, 0.55, and 0.26 g cm$^{-3}$, respectively.

**Table 2.** Surface-to-volume ratio of nanoporous double gyroid structures.

| Sample | $\phi$[a)] | $d_{100}$ [nm] | $V_{bulk}$[b)] [$nm^3$] | S[c)] [$nm^2$] | $S/V_{bulk}$ [$nm^{-1}$] | $S/V_p$[d)] [$nm^{-1}$] |
|---|---|---|---|---|---|---|
| PG | 76% | 381 | $5.5 \times 10^7$ | $6.1 \times 10^5$ | 0.0111 | 0.0145 |
| NG | 47% | 379 | $5.4 \times 10^7$ | $7.7 \times 10^5$ | 0.0141 | 0.0300 |
| HG | 23% | 378 | $5.4 \times 10^7$ | $1.4 \times 10^6$ | 0.0251 | 0.119 |

a) Volume fraction of the preserved volume fraction of the matrix (PG) or network (NG and HG); b) Bulk volume ($V_{bulk}$) = $(d_{100})^3$; c) Surface area (S) is from computational simulation; d) Volume of the preserved matrix or network ($V_p$) = $\phi \times V_{bulk}$.

because of the high porosity and the uniformity of the HG networks at the nanoscale. Notably, even for a large film thickness of 4 µm, the HG film retained (Figure 5c) its high transmittance of 98%. As displayed in Figure 5d, the HG film placed on a poly(ethylene terephthalate) (PET) substrate exhibited high transmittance of visible light. The development of flexible displays or devices currently can be divided into four stages. The first stage consists of fixed-curve flexible devices, the second stage involves bendable and rollable technology with a bending radius of 0.3 to 1.5 cm, the third stage is characterized by foldable technology with a smaller bending radius (0.05 to 0.3 cm), and the fourth stage is fully flexible technology that can be folded and stretched in any direction. Therefore, the film flexibility was measured by bending radius, as shown in Figure S10 (Supporting Information). The bending radius of the HG-structured film can reach a minimum value of 0.2 cm without the formation of cracks, indicating that we have achieved the standard of the third stage. Therefore, dual-extractable ternary nanocomposites can provide interesting self-assembled nanoporous structures for the fabrication of flexible optical transmittance materials and also for use as templates for preparing 3D ordered inorganic nanomaterials of the high surface-to-volume ratio.

With the high porosity and highly interconnected 3-D nanodomains, these lightweight nanomaterials should exhibit a significant elevation of specific modulus. The average values of reduced elastic modulus (Er) were determined using a nanoindenter. For a set of ten independent measurements, the averaged Er values of the DG, PG, NG, and HG are 3.54 ± 0.25, 3.36 ± 0.18, 4.16 ± 0.13, and 3.61 ± 0.37 GPa, respectively (Figure 5e,f). In contrast to the neat PMMA-*b*-P2VP (Er = 4.58 ± 0.28 GPa in Figure S11, Supporting Information), the decrease of the $Er_{DG}$ ternary nanocomposite is due to the softening of the P2VP block chains induced by the depression of the $T_{g,P2VP}$ to 58.1 °C due to blending with the mesogen in contrast to the normal $T_g$ of P2VP (100.7 °C) in the neat PMMA-*b*-P2VP BCP (Figure S12a, Supporting Information). After the degradation of the minor PMMA network, the $Er_{PG}$ becomes lower than the $Er_{DG}$ due to the formation of the porous structure. After solvent-extracting the mesogens, $Er_{NG}$ of 4.16 GPa is higher than the $Er_{DG}$ due to the return of the $T_{g,P2VP}$ to 100.2 °C (Figure S12a, Supporting Information). Similar variations of the $T_g$ are obtained in blends of the homopolymer P2VP and mesogens. For a blend with a molar ratio of 0.45, the $Er_{P2VP(m)}$ of 3.42 ± 0.23 GPa in the $P2VP(m)_{0.45}$ sample is lower than that of the neat P2VP (4.64 ± 0.25 GPa) in Figure S11 (Supporting Information), due to the depression of the $T_{g,P2VP}$ (58.5 °C) in the $P2VP(m)_{0.45}$ in contrast to 98.4 °C of the P2VP homopolymer (Figure S12b, Supporting Information). Although the HG possesses the lowest structural volume fraction ($\phi_{air}$ = 0.77), the $Er_{HG}$ of 3.61 ± 0.37 GPa is only slightly smaller than that of the $Er_{NG}$ (4.16 ± 0.13 GPa) ($\phi_{air}$ = 0.53). Because the density of the HG largely decreases to 0.26 (g $cm^{-3}$), the HG-structured material possesses a highest specific modulus of 13.37 (GPa $cm^3$ $g^{-1}$), which is ≈1.8 times, 3.3 times and 4.2 times higher than those of the NG (7.56 GPa $cm^3$ $g^{-1}$), PG (4.10 GPa $cm^3$ $g^{-1}$) and DG (3.19 GPa $cm^3$ $g^{-1}$), respectively. We suggest that the maintaining Er value of HG without substantial reduction can be ascribed to the presence of highly interconnected ordered nanonetworks. These ordered nanonetworks provide the uniform dissipation of applied stress through bicontinuous nanodomains, resulting in less susceptibility to the influence of increased porosity.

## 3. Conclusion

We have fabricated flexible, lightweight NG, PG, and HG nanoporous gyroid structures from a single dual-extractable nanocomposite via simple and efficient processing conditions. This new dual-extractable nanocomposite approach introduces physically-bonded mesogens to the P2VP blockchains and allows the fabrication of both PG and NG nanotemplates through UV depolymerization of the minority PMMA blocks or solvent-extraction of the incorporated mesogens from the majority P2VP-mesogen matrix, respectively. Except for PG and NG, a novel nanoporous HG structure of extremely low structural volume and highest porosity and surface-to-volume ratio can be generated, which consists of interpenetrating double hollow tubular networks of the remaining P2VP component. Because of the asymmetric chain conformation of the mesogen-associated P2VP blockchains, a minimum volume fraction (24%) of the DG minority network was obtained for the first time. To the best of our knowledge, this is the first work to fabricate a flexible polymer-based HG nanostructure of extremely high porosity and minimum structural volume from self-assembly of diblock copolymers. In contrast to typical PG and NG structures from the self-assembly of semi-degradable diblock copolymers, this unique HG structure from the ternary nanocomposite could exhibit the significantly increased porosity and better specific modulus while remaining transparent even for a relatively thick film of 4 µm. The surface-to-volume ratio of the HG is increased to four times the NG and 8.2 times the PG. The lightweight and high-porosity HG also exhibits robust mechanical behavior with a specific reduced modulus of 13.4 GPa×$cm^3$ $g^{-1}$, almost 1.8 times that of NG, 3.3 times that of PG, and 4.2 times that of DG. The resultant HG composed of the hydrophilic P2VP is quite distinct from the typical hydrophobic nanoporous structure such as the PS-based nanoporous structure. This unique hydrophilic DG-structured template featuring the minimum structural volume, strong polarity, and tunable affinity has a high potential to produce inorganic or organic nanomaterials with greatly enhanced optical and specific mechanical properties such as specific modulus.

## 4. Experimental Section

*Materials*: The PMMA-*b*-P2VP block copolymer was purchased from Polymer Source, Inc. (Doval, Canada.) The number-average molecular

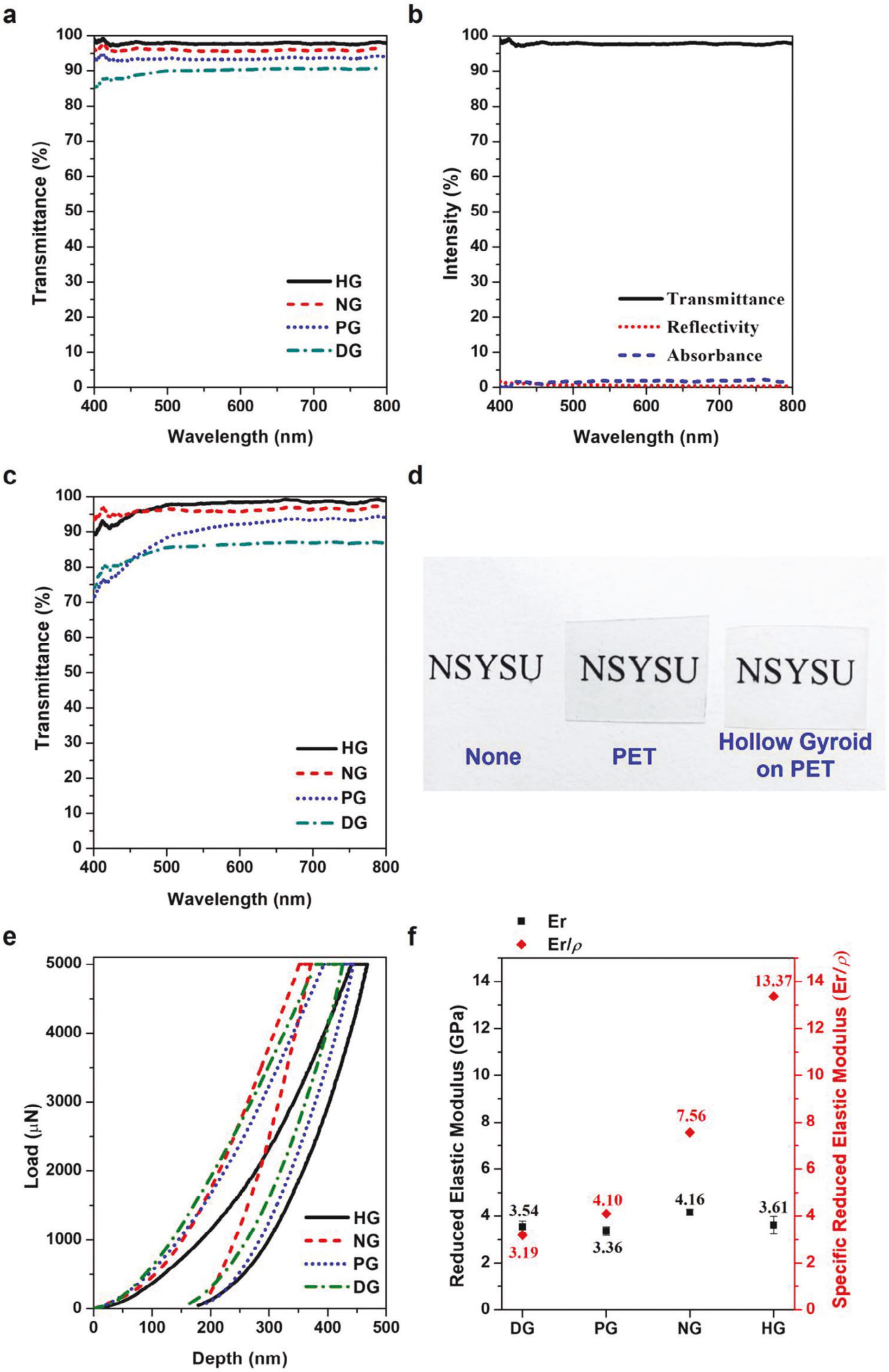

**Figure 5.** Comparison of the properties of the four different DG structures. a) Optical transmittance of the various DG materials (film thickness: 300 nm). b) Reflectivity, absorption and transmittance of the HG film with a film thickness of 300 nm. c) Transmittance spectra of the DG and PG, NG, and HG films with a thickness of 4 μm. d) Photographs of a 4 μm-thick nanoporous HG film coated on a PET substrate and a neat PET film. e) Load–depth profiles with a maximum load of 5000 μN for the various DG structures. f) Averaged Er values measured using a flat-punch probe of 10 μm diameter at room temperature for films with 5 μm in thickness.

weights of the PMMA and P2VP blocks were 170 and 160 kDa, respectively. The degree of polymerization of the PMMA and P2VP blockchains was 1700 and 1524, respectively. The PDI of the PMMA-*b*-P2VP BCP is 1.10. The volume fraction of the PMMA was calculated to be 0.51 based on the PMMA and P2VP densities of 1.188 and 1.153 g cm$^{-3}$, respectively. The P2VP homopolymer with a number-average molecular weight of 152 kDa was used as received from Sigma–Aldrich. The cholesteric liquid crystal mesogen of cholesteryl hemisuccinate (abbreviated as m) was used as received from Sigma–Aldrich. The molecular weight of the mesogen was 486.73 Da and its density was 1.06 g cm$^{-3}$.

*Sample Preparation*: All bulk samples were cast from solutions of 1,1,2-trichloroethane (TCE) containing mixtures (5 wt.%) of the copolymer and mesogens of various molar ratios. The as-cast bulk samples were dried slowly at 25 °C and were further dried in a vacuum oven to remove the residual solvent. To fabricate the PG structure, the PMMA-*b*-P2VP(m)$_{0.45}$ sample was exposed to UV irradiation of 254 nm for 4 h under argon to decompose the PMMA blockchains. After UV irradiation, we immersed the exposed PMMA-*b*-P2VP(m)$_{0.45}$ nanocomposite into o-xylene, a poor solvent for both the P2VP block and the mesogen, to remove the photodegraded PMMA blocks. For the NG structure, the PMMA-*b*-P2VP(m)$_{0.45}$ sample was immersed in cold methanol at 4 °C for 1 h to remove mesogenic molecules. To obtain the HG structure, the solvent-extracting process and the UV irradiation were conducted in sequence.

*Characterization*: The bulk samples were sectioned into 100 nm-thick slices for TEM observation, using an ultra-microtome (Leica EM UC7) at 25 °C. Bright-field TEM images employing mass-thickness contrast were obtained using a transmission electron microscope (JEOL JEM-2100) operated at an accelerating voltage of 200 kV. The sliced samples were stained with $I_2$ vapor for 1 h to increase the contrast between the PMMA and P2VP domains; the P2VP microdomains appeared dark after staining with $I_2$ whereas the PMMA microdomains appeared bright[38] Medium-angle X-ray diffraction (MAXD) and small-angle X-ray scattering (SAXS) measurements were respectively performed at the BL23A beamline of the Taiwan light source (TLS) and the BL25A beamline of the Taiwan photon source (TPS) at the National Synchrotron Radiation Research Center (NSRRC). MAXD and SAXS were conducted at the wavelengths of 0.9678 and 0.8265 Å, respectively. The SAXS pattern was collected with an area detector (Pilatus 1M-F) that was corrected for electronic noise, transmission, background scattering, and detector sensitivity. The area detector was calibrated for absolute scattering intensity of SAXS by using high-density polyethylene; silver behenate was used for the calibration of scattering wavevector $q$ defined by $4\pi\lambda^{-1}\sin\theta$ with the scattering angle of $2\theta$. Field emission scanning electron microscopy (FESEM) images of uncoated samples were recorded with a field-emission scanning electron microscope (ZEISS GeminiSEM 450) operated at an accelerating voltage of 1 keV. Transmittance and reflectivity measurements were conducted by a UV–vis spectroscopy (Jasco J-1700 circular dichroism spectroscopy) and an optical microscope (ESPA N-800 M) equipped with a fiber-optic spectrometer (B&W Teki-trometer). Nanoindentation measurements were conducted using a nanoindenter (TI900 TriboIndenter, Hysitron Inc.) for the examination of at least 10 different positions. The load (up to a maximum of 5000 µN) was applied by a flat diamond indenter with 10 µm diameter at the same loading and unloading rate of 60 µN s$^{-1}$. The reduced modulus of the test sample can be calculated from the load-displacement profile based on the following equation:

$$E_r = \frac{S'}{D} \tag{1}$$

where *Er* is reduced modulus and S' is stiffness (slope of the unloading curve). *D* represents the diameter of the diamond flat indenter. For recording the reduced modulus, the deformation of the diamond indenter is negligible. Therefore, the reduced modulus is a representative value for mechanical performance. The film thickness is 5 µm, and the depth of indentation (<500 nm) was less than 10% of the total film thickness.

## Supporting Information

Supporting Information is available from the Wiley Online Library or from the author.

## Acknowledgements

The authors appreciate the help of Hsien-Tsan Lin and Tsai-Jung Yen of the Regional Instruments Center of National Sun Yat-Sen University for the TEM (ID: EM022600) and FESEM (ID: EM001500) experiments; Yu-Shan Huang, Jhih-Min Lin, and Chun-Yu Chen of the National Synchrotron Radiation Research Center (Taiwan) for the synchrotron experiments; and Ministry of Science and Technology of the Republic of China, Taiwan, for financial support (MOST108-2628-E-110-002-MY3 and MOST111-2221-E-110-001). The research at TAMU (ELT) was supported by a grant from NSF DMR-2105296.

## Conflict of Interest

The authors declare no conflict of interest.

## Data Availability Statement

The data that support the findings of this study are available from the corresponding author upon reasonable request.

## Keywords

dual-extractable, gyroid, hollow nanonetworks, metamaterials, nanoporous

Received: August 28, 2023
Revised: October 18, 2023
Published online: November 20, 2023

---

[1] D. A. Hajduk, P. E. Harper, S. M. Gruner, C. C. Honeker, G. Kim, E. L. Thomas, L. J. Fetters, *Macromolecules* **1994**, *27*, 4063.
[2] S. Foerster, A. K. Khandpur, J. Zhao, F. S. Bates, I. W. Hamley, A. J. Ryan, W. Bras, *Macromolecules* **1994**, *27*, 6922.
[3] L. Xiang, Q. Li, C. Li, Q. Yang, F. Xu, Y. Mai, *Adv. Mater.* **2023**, *35*, 2207684.
[4] A. M. Urbas, M. Maldovan, P. Derege, E. L. Thomas, *Adv. Mater.* **2002**, *14*, 1850.
[5] M. R. J. Scherer, *Double-Gyroid-Structured Functional Materials Synthesis and Applications*, Springer, University of Cambridge, UK **2013**.
[6] E.-L. Lin, W.-L. Hsu, Y.-W. Chiang, *ACS Nano* **2018**, *12*, 485.
[7] V. Z.-H. Chan, J. Hoffman, V. Y. Lee, H. Iatrou, A. Avgeropoulos, N. Hadjichristidis, R. D. Miller, E. L. Thomas, *Science* **1999**, *286*, 1716.
[8] T. Hashimoto, K. Tsutsumi, Y. Funaki, *Langmuir* **1997**, *13*, 6869.
[9] E. J. W. Crossland, M. Kamperman, M. Nedelcu, C. Ducati, U. Wiesner, D.-M. Smilgies, G. E. S. Toombes, M. A. Hillmyer, S. Ludwigs, U. Steiner, H. J. Snaith, *Nano Lett.* **2009**, *9*, 2807.
[10] M. R. J. Scherer, L. Li, P. M. S. Cunha, O. A. Scherman, U. Steiner, *Adv. Mater.* **2012**, *24*, 1217.
[11] M. W. Matsen, F. S. Bates, *Macromolecules* **1996**, *29*, 1091.
[12] X. Feng, C. J. Burke, M. Zhuo, H. Guo, K. Yang, A. Reddy, I. Prasad, R.-M. Ho, A. Avgeropoulos, G. M. Grason, E. L. Thomas, *Nature* **2019**, *575*, 175.
[13] H.-Y. Hsueh, H.-Y. Chen, M.-S. She, C.-K. Chen, R.-M. Ho, S. Gwo, H. Hasegawa, E. L. Thomas, *Nano Lett.* **2010**, *10*, 4994.

[14] H.-Y. Hsueh, Y.-C. Ling, H.-F. Wang, L.-Y. C. Chien, Y.-C. Hung, E. L. Thomas, R.-M. Ho, *Adv. Mater.* **2014**, *26*, 3225.
[15] T. Hashimoto, Y. Nishikawa, K. Tsutsumi, *Macromolecules* **2007**, *40*, 1066.
[16] A. S. Finnemore, M. R. J. Scherer, R. Langford, S. Mahajan, S. Ludwigs, F. C. Meldrum, U. Steiner, *Adv. Mater.* **2009**, *21*, 3928.
[17] S. Vignolini, N. A. Yufa, P. S. Cunha, S. Guldin, I. Rushkin, M. Stefik, K. Hur, U. Wiesner, J. J. Baumberg, U. Steiner, *Adv. Mater.* **2012**, *24*, OP23.
[18] L. Guo, Z. Zhong, Y. Wang, *Adv. Mater. Interfaces* **2016**, *3*, 1600017.
[19] C.-S. Wu, P.-Y. Tsai, T.-Y. Wang, E.-L. Lin, Y.-C. Huang, Y.-W. Chiang, *Anal. Chem.* **2018**, *90*, 4847.
[20] J. Ruokolainen, G. T. Brinke, O. Ikkala, *Adv. Mater.* **1999**, *11*, 777.
[21] S. Valkama, T. Ruotsalainen, A. Nykänen, A. Laiho, H. Kosonen, G. Ten Brinke, O. Ikkala, J. Ruokolainen, *Macromolecules* **2006**, *39*, 9327.
[22] J. T. Korhonen, T. Verho, P. Rannou, O. Ikkala, *Macromolecules* **2010**, *4*, 1507.
[23] A. J. Soininen, I. Tanionou, N. Ten Brummelhuis, H. Schlaad, N. Hadjichristidis, O. Ikkala, J. Raula, R. Mezzenga, J. Ruokolainen, *Macromolecules* **2012**, *45*, 7091.
[24] T. Thurn-Albrecht, R. Steiner, J. Derouchey, C. M. Stafford, E. Huang, M. Bal, M. Tuominen, C. J. Hawker, T. P. Russell, *Adv. Mater.* **2000**, *12*, 787.
[25] I. Vukovic, T. P. Voortman, D. H. Merino, G. Portale, P. Hiekkataipale, J. Ruokolainen, G. Ten Brinke, K. Loos, *Macromolecules* **2012**, *45*, 3503.
[26] I. M. Lin, C. M. Chou, M. C. Li, R. H. Guo, C. K. Lee, H. J. Li, Y. W. Chiang, Y. H. Lin, Y. C. Lee, C. J. Su, U. S. Jeng, W. T. Chuang, *J. Mater. Chem. C* **2020**, *8*, 1923.
[27] S. Salvatore, S. Vignolini, J. Philpott, M. Stefik, U. Wiesner, J. J. Baumberg, U. Steiner, *Nanoscale* **2015**, *7*, 1032.
[28] Y. H. Kim, J.-Y. Bae, J. Jin, B.-S. Bae, *ACS Appl. Mater. Interfaces* **2014**, *6*, 3115.
[29] W. Wei, Y. Liu, H. Xiong, *ACS Macro Lett.* **2014**, *3*, 892.
[30] F. Liu, M. Prehm, X. Zeng, C. Tschierske, G. Ungar, *J. Am. Chem. Soc.* **2014**, *136*, 684.
[31] T. Ichikawa, M. Yoshio, A. Hamasaki, S. Taguchi, F. Liu, X.-B. Zeng, G. Ungar, H. Ohno, T. Kato, *J. Am. Chem. Soc.* **2012**, *134*, 2634.
[32] S. R. Nowak, K. K. Lachmayr, K. G. Yager, L. R. Sita, *Angew. Chem., Int. Ed.* **2021**, *60*, 8710.
[33] H. Kim, M. M. L. Arras, J. P. Mahalik, W. Wang, D. M. Yu, S. Chernyy, M. Goswami, R. Kumar, B. G. Sumpter, K. Hong, G. S. Smith, T. P. Russell, *Macromolecules* **2018**, *51*, 7491.
[34] W. A. Kuhlman, E. A. Olivetti, L. G. Griffith, A. M. Mayes, *Macromolecules* **2006**, *39*, 5122.
[35] M. W. Matsen, F. S. Bates, *J. Polym. Sci. B Polym. Phys.* **1997**, *35*, 945.
[36] L. Liberman, M. L. Coughlin, S. Weigand, F. S. Bates, T. P. Lodge, *Macromolecules* **2022**, *55*, 2821.
[37] W. Wei, L. Samad, J. W. Choi, Y. Joo, A. Way, M. S. Arnold, S. Jin, P. Gopalan, *Chem. Mater.* **2016**, *28*, 4017.
[38] E. L. Thomas, Y. Talmon, *Polymer* **1978**, *19*, 225.